Calculation of Flowfields in Side-Inlet Ramjet Combustors with an Algebraic Reynolds Stress Model

T.-M. Liou* and Y.-H. Hwang†
National Tsing Hua University, Hsin-Chu, Taiwan, Republic of China

Calculations have been made of the three-dimensional, isothermal, turbulent flowfield development in two side-inlet dump combustor configurations for Reynolds numbers 2.6×10^4 and 2.7×10^5, respectively. The governing partial differential equations are solved numerically with an algebraic Reynolds stress turbulence model. The calculated flow structure is presented in terms of mean velocity profiles, swirl intensity, total pressure loss, and the fractions of the inlet mass flow rate transported into and out of the dome region. In addition, the calculated results are compared with the reported laser-Doppler velocimetry data and flow visualization photographs. Reasonable agreement is obtained. Furthermore, the present calculations have shown an improvement over the previous work in the prediction of the vortex pattern in the dome region.

Nomenclature

A = surface area
A_{in} = cross-section area at the inlet port
$A(X_c^*)$ = cross-section area at a given X_c^*
C_{A1}, C_{A2}, C_1, C_2, C_μ = constants in turbulence model
$\tilde{C}_{A1}$, $\tilde{C}_{A2}$ = modified constants for C_{A1} and C_{A2}, respectively
D_c = combustor diameter
E_{in} = the flux of the total mean energy at inlet
$E(X_c^*)$ = the axial flux of total mean energy at a given X_c^*
k = turbulence kinetic energy
K_0 = loss coefficient
L_d = dome height of combustor
$\dot{m}_{in}$ = inlet flow rate
$\dot{m}_{ri}$ = reversal flow rate in dome region
$\dot{m}_{ro}$ = forward flow rate in dome region
N = unit vector normal to surface area A
P = pressure
$\tilde{P}_{ij}$, P_{ij} = defined as

$$\tilde{P}_{ij} = -\left[\overline{(u_i u_m)}_B \frac{\partial U_j}{\partial X_m} + \overline{(u_j u_m)}_B \frac{\partial U_i}{\partial X_m}\right]$$

$$P_{ij} = -\left[\overline{(u_i u_m)}_d \frac{\partial U_j}{\partial X_m} + \overline{(u_j u_m)}_d \frac{\partial U_i}{\partial X_m}\right]$$

$\tilde{P}_k$, P_k = defined as

$$\tilde{P}_k = \tfrac{1}{2}\tilde{P}_{ii},\ P_k = \tfrac{1}{2}P_{ii}$$

R_c = combustor radial coordinate
R_c^* = nondimensional combustor radial coordinate

$$R_c^* = R_c/(D_c/2)$$

Re_c = combustor Reynolds number

$$Re_c = \rho U_{ref} D_c/\mu_\ell$$

SI = swirl intensity
U = axial mean velocity
U_{ref} = combustor bulk mean velocity
V = radial mean velocity
$\boldsymbol{V}$ = velocity vector
W = azimuthal mean velocity
X_c^* = nondimensional combustor axial coordinate

$$X_c \le 0,\ X_c^* = X_c/L_d$$

$$X_c \ge 0,\ X_c^* = X_c/D_c$$

X_c = combustor axial coordinate
y = distance from wall
ϵ = dissipation rate of turbulence kinetic energy
θ_c = combustor azimuthal coordinate
ρ = fluid density
μ_ℓ = molecular dynamic viscosity
μ_t = turbulent dynamic viscosity
σ_k, σ_ϵ = turbulent Prandtl number of k and ϵ, respectively

Introduction

CALCULATIONS have been performed on the three-dimensional isothermal flowfield development in dual-inlet side-dump combustors. Side-dump combustors are being investigated as a possible alternative to coaxial-dump combustors for lightweight propulsion systems such as liquid-fueled ramjets and solid ducted rockets. It is obvious that the complex flow patterns may have significant influences on the fuel mixing and combustion charateristics in the combustors. Therefore, analytical or experimental studies of the detailed fluid dynamic process are necessary.

Shahaf et al.[1] studied the flowfield in a two-dimensional side-dump square combustor model of a liquid-fueled ramjet both analytically and experimentally. Results were presented in terms of axial mean velocity at one or four axial stations. Large discrepancies between the measured and calculated profiles were found along the combustor axis and in the recirculating zones. Stull et al.[2] and Vanka et al.[3] investigated the flowfield characteristics of a three-dimensional side-inlet dump combustor by varying the position of the dome plate and the angle of the side inlets. Their calculated results agreed

Presented as Paper 88-3010 at the AIAA/ASME/SAE/ASEE 24th Joint Propulsion Conference, Boston, MA, July 11-13, 1988; received May 31, 1988; revision received Jan. 6, 1989.

*Professor, Power Mechanical Engineering Department.
†Graduate Student, Power Mechanical Engineering Department.

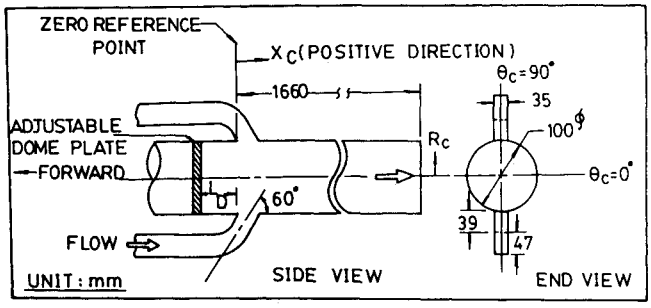

Fig. 1 Sketch of configuration, coordinate system, and dimensions of dual-inlet side-dump combustor.

qualitatively with the flow visualization in a water tunnel; however, a vortex pattern in the dome region shown by flow visualization was not seen in their calculations. Recently, Vanka et al.[4] performed further calculations of the three-dimensional reacting flowfield in a side-dump combustor with gaseous fuel injected through the dome plate and air induced through the two 45-deg ducts. However, as pointed out by Vanka et al.,[4] there are no experimental data to validate the turbulence and combustion models in their calculations. In view of the lack of quantitative experimental data with which to compare numerical predictions, Liou and Wu performed detailed mean velocity and turbulence intensity measurements in curved 60-deg inlet ducts[5] and in a three-dimensional side-dump combustor with a circular cross section[6] using laser-Doppler velocimetry (LDV).

The brief literature survey just given suggests that a computational study of side-dump combustor flowfields, including comparisons with available experimental results, would be worthwhile. Consequently, this paper presents computational results for two different ramjet configurations that were studied by Liou and Wu[6] and Stull et al.,[2] respectively. The main differences between the two cases are as follows: For the former, the azimuthal angle between the two side inlets is 180 deg, the angle of the side inlets with respect to the combustor axis is 60 deg, air is the working medium, and the Reynolds number is 2.6×10^4 (see Fig. 1). For the latter, the azimuthal angle is 90 deg, the angle of the side inlets is 45 deg, water is the working medium, and the Reynolds number is 2.7×10^5. The experimental results obtained for these two cases would be a useful test of the present calculations. The turbulence model adopted in the present study is the algebraic Reynolds stress model,[7] which is a modified version of the k-ϵ turbulence model and has not been previously applied to simulate the flowfield in a side-dump combustor in the literature.

In the following sections, the details of theoretical treatment, including the equations solved, boundary conditions specified, and solution algorithm used, are stated. The computed flow patterns are subsequently discussed. Then, the comparisons with LDV measurement and with previous calculation and flow visualization results are given.

Theoretical Treatment

The computations were performed by numerically solving the fully elliptic three-dimensional Navier-Stokes equations, since flow recirculation was expected to be three-dimensional. To simplify the problem, the flow was considered to be isothermal, incompressible, and steady-state in the mean.

Mean Flow Equations

In order to make the analysis of turbulent flow problems computationally tractable, it is usual to express the instantaneous value of any turbulent flow property Φ, say, in terms of a time-averaged component $\bar{\Phi}$, and a fluctuating component ϕ, such that $\Phi = \bar{\Phi} + \phi$. Therefore, the time-averaged equations for conservation of mass and momentum can be expressed in tensor notation as

$$\frac{\partial U_i}{\partial X_i} = 0 \tag{1}$$

$$\frac{\partial}{\partial X_j}(\rho U_i U_j) = -\frac{\partial P}{X_i} + \frac{\partial}{\partial X_j}\left[\mu_t\left(\frac{\partial U_i}{\partial X_j} + \frac{\partial U_j}{\partial X_i}\right) - \rho\overline{u_i u_j}\right] \tag{2}$$

Note that the body force term has been neglected in the momentum equation, and the turbulence correlation $\overline{u_i u_j}$ is the time-average $u_i u_j$ and stands for the Reynolds stresses that must be modeled to close Eqs. (1) and (2).

Turbulence Model

The algebraic Reynolds stress equation proposed by Ljuboja and Rodi[7] is adopted and is expressed as

$$\frac{\overline{u_i u_j}}{k}\left(-\overline{u_m u_n}\frac{\partial U_m}{\partial X_n} - \epsilon\right) = -\left(\overline{u_i u_m}\frac{\partial U_j}{\partial X} + \overline{u_j u_m}\frac{\partial U_j}{\partial X_m}\right) - \frac{2}{3}\delta_{ij}\epsilon - C_{A1}\frac{\epsilon}{k}\left(\overline{u_i u_j} - \frac{2}{3}\delta_{ij}k\right) - C_{A2}\left[-\left(\overline{u_i u_m}\frac{\partial U_j}{\partial X_m} + u_j u_m\frac{\partial U_i}{\partial X_m}\right) + \frac{2}{3}\delta_{ij}\overline{u_m u_n}\frac{\partial U_n}{\partial X_m}\right] \tag{3}$$

where $C_{A1} = 1.5$ and $C_{A2} = 0.6$ are model constants. In the present calculation, the Reynolds stress is decomposed into a Boussinesq part and a deviation part to simplify the computational procedure:

$$-\rho\overline{u_i u_j} = (-\rho\overline{u_i u_j})_B + (-\rho\overline{u_i u_j})_d \tag{4}$$

The Boussinesq part of Reynolds stress[8] is

$$(-\rho\overline{u_i u_j})_B = \mu_t\left(\frac{\partial U_i}{\partial X_j} + \frac{\partial U_j}{\partial X_i}\right) - \frac{2}{3}\delta_{ij}\rho k \tag{5}$$

where δ_{ij} is the Kronecker-Delta function, and μ_t is the turbulent viscosity that may be related to the kinetic energy of turbulence k and its dissipation rate ϵ by the following relationship:

$$\mu_t = C_\mu \rho k^2/\epsilon \tag{6}$$

where $C_\mu = 0.09$[9] is a constant of the model. The six nonlinear algebraic equations of $(\overline{u_i u_j})_d$ are listed in the Appendix. The differential equations for k and ϵ are

$$\frac{\partial}{\partial X_j}(\rho U_j k) = \frac{\partial}{\partial X_j}\left[(\mu_l + \mu_t/\sigma_k)\frac{\partial k}{\partial X_j}\right] - \rho\overline{u_i u_j}\frac{\partial U_i}{\partial X_j} - \rho\epsilon \tag{7}$$

$$\frac{\partial}{\partial X_j}(\rho U_j \epsilon) = \frac{\partial}{\partial X_j}\left[(\mu_l + \mu_t/\sigma_\epsilon)\frac{\partial \epsilon}{\partial X_j}\right] - C_1\frac{\epsilon}{k}\rho\overline{u_i u_j}\frac{\partial U_i}{\partial X_j} - C_2\rho\epsilon^2/k \tag{8}$$

where $C_1 = 1.44$ and $C_2 = 1.92$ are further model constants. Furthermore, $\sigma_k = 1.0$ and $\sigma_\epsilon = 1.217$ are turbulent Prandtl numbers for k and ϵ, respectively. Equations (5) and (6) can be substituted into Eqs. (2), (3), (7), and (8) to form a set of equations that have the same number of equations and unknowns. Thus, the closure problem of the turbulent flow calculations is completed.

Boundary Conditions

The above set of three-dimensional (R_c^*-θ_c-X_c^* and V-W-U) elliptic partial differential equations has to be solved with the following boundary conditions (see Figs. 1 and 2):

1) Symmetric planes ($\theta_c = 0$ deg and $\theta_c = 90$ deg)

$$\frac{\partial U}{\partial \theta_c} = \frac{\partial V}{\partial \theta_c} = \frac{\partial k}{\partial \theta_c} = \frac{\partial \epsilon}{\partial \theta_c} = 0, \qquad W = 0$$

2) Combustor axis ($R_c = 0$)

$$\frac{\partial U}{\partial R_c} = \frac{\partial k}{\partial R_c} = \frac{\partial \epsilon}{\partial R_c} = 0, \qquad V = W = 0$$

3) Exit

$$\frac{\partial U}{\partial X_c} = \frac{\partial k}{\partial X_c} = \frac{\partial \epsilon}{\partial X_c} = 0, \qquad V = W = 0$$

In this study, the location of the computational downstream boundary was determined from the measured results or from the computational test. In fact, the computational test showed that there is no noticeable change in the flowfield as long as the location of the exit plane is far enough to allow the flow to become unidirectional.

4) Inlet

$$U = \text{measured } U_{\text{in}}, \qquad V = \text{measured } V_{\text{in}}$$

$$W = \text{measured } W_{in}$$

$$k = \text{measured } k_{\text{in}}, \qquad \epsilon = \epsilon_{\text{in}} = k_{\text{in}}^{3/2}/(B \cdot \lambda)$$

where B = inlet-duct width = $D_c/2$ and $\lambda = 0.005$.

5) Walls

$$U = 0, \qquad V = 0, \qquad W = 0$$

Since the k and ϵ equations are valid only in those regions that are strongly turbulent, i.e., in regions where the eddy diffusivity overwhelms the molecular diffusivity, it is not applicable in the viscous sublayer. In the other way, the steep change of flow properties in the wall region needs an extremely fine grid arrangement and makes the computational efforts unpractical. Therefore, in this study, the near-wall region was simulated by a semi-empirical two-zone model, i.e., viscous sublayer and fully turbulent zone, and wall function[9] was used to bridge the viscous sublayer. Futhermore, the constants C_{A1} and C_{A2} in the algebraic Reynolds stress equation (3) are substituted by $\tilde{C}_{A1}$ and $\tilde{C}_{A2}$ with the following relationship,[10] respectively:

$$\tilde{C}_{A1} = C_{A1} + 0.125k^{3/2}/(\epsilon y) \tag{9}$$

$$\tilde{C}_{A2} = C_{A2} + 0.15k^{3/2}/(\epsilon y) \tag{10}$$

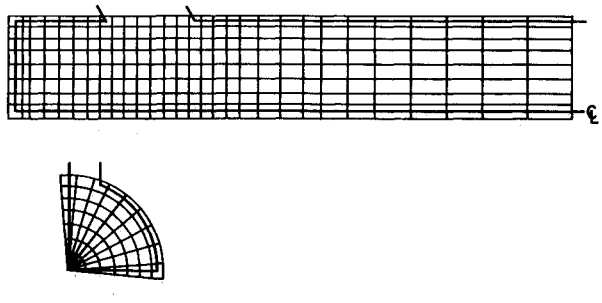

Fig. 2 Grid system for finite-difference computation.

where y is the distance between the node point and its neighboring wall.

Numerical Scheme

The solution of the previous partial differential equations along with the boundary conditions is obtained by using the iterative finite-difference scheme based on the SIMPLE (semi-implicit pressure-linked equations) algorithm of Patankar and Spalding.[11] The partial differential equations are integrated over small discrete control volumes that are formed by the grid system and are converted to a set of nonlinear algebraic eqautions. A staggered grid system is employed. Figure 2 shows the grid arrangement for all scalar variables. The nodes of the velocity grid are located midway between the scalar grid nodes to represent the true convective quantities across the boundary of such control volumes. The power-law scheme[12] is applied to formulate the total fluxes, including convective and diffusive terms, across the faces of the control volumes.

The solutions procedure is initiated with guesses for the velocity and pressure fields and then proceeds with line-by-line iteration. After each sweep over the solution domain, adjustments for the pressure field are made to satisfy the continuity along each line of cells. These adjustments in turn destroy the compliance of the velocities and pressure fields with the momentum equations. Further iterations are thus needed until the continuity and momentum equations are simultaneoulsy satisfied to the requisite degree of accuracy. The tolerance of the normalized mass and momentum residuals are typically from 0.005 to 0.001; k and ϵ are also solved line by line simultaneously with the mean velocity distribution. To solve the system of nonlinear algebraic equations deduced from the algebraic Reynolds stress model, a global convergent secant method employing Broyden update with an analytical Jacobian matrix[13] is used. To prevent numerical instability, successive changes of the flow variables are under-relaxed with their old values. The under-relaxation factors are 0.5 for U, V, W, k, ϵ, μ_t, and 0.3 for P, $(\overline{u_i u_j})_d$, respectively.

The calculations for the case of Liou and Wu[6] were made using a $9 \times 10 \times 40$ grid (Fig. 2) in the radial, azimuthal, and axial directions, respectively. A large number of grid points were placed in the areas where steep variations in velocities were revealed from the previous experimental results. Because of the large computing resources required, thorough grid inde-

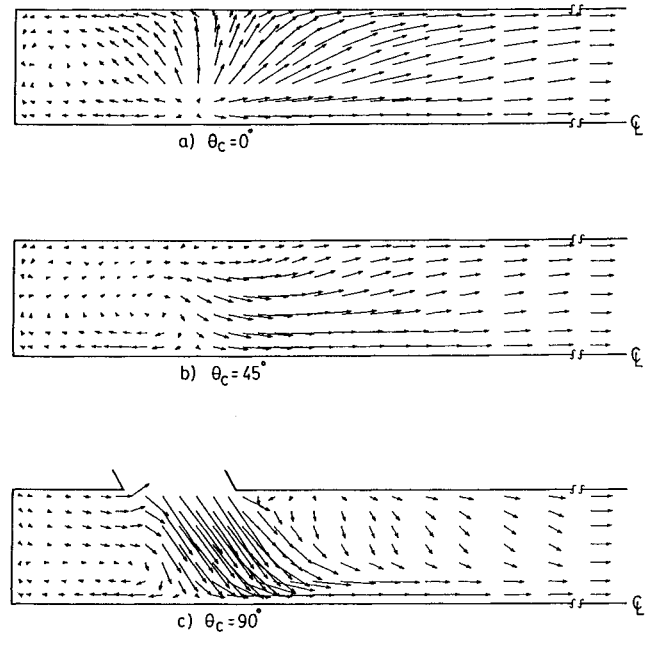

Fig. 3 Vector plots of flow patterns in planes of constant θ_c.

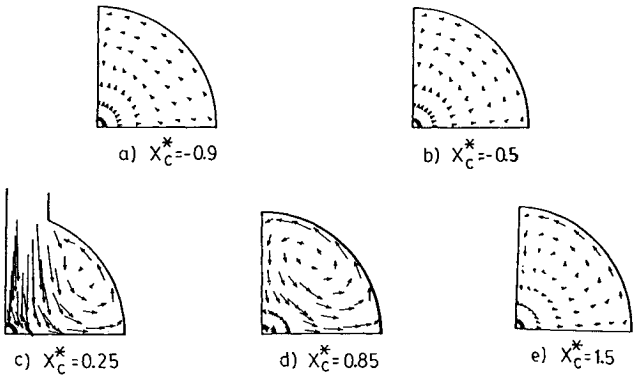

Fig. 4 Vector plots of azimuthal flow structure at various X_c^*.

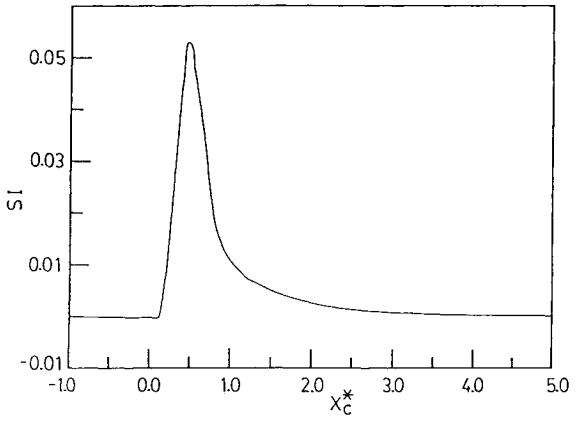

Fig. 5 Swirl intensity distribution.

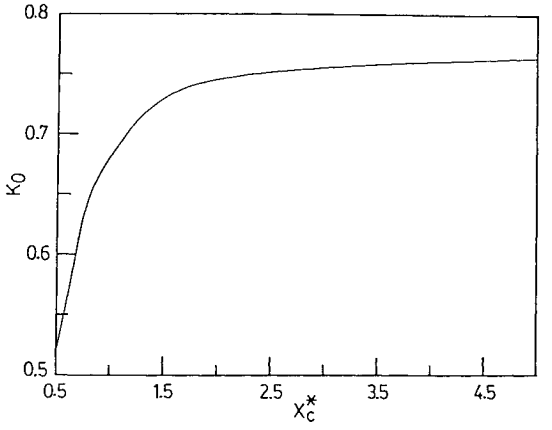

Fig. 6 Distribution of dimensionless total pressure loss.

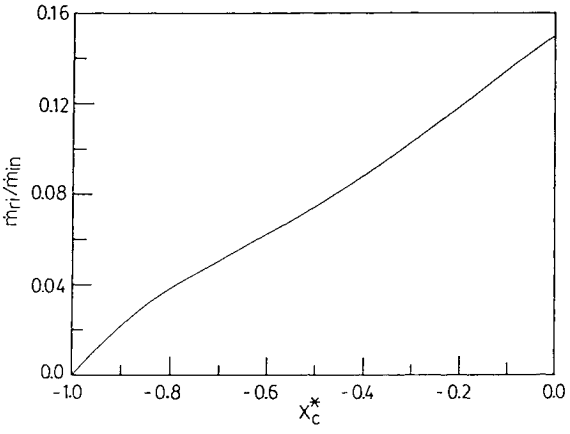

Fig. 7 Fraction of inlet mass flow transported into the dome region vs X_c^*.

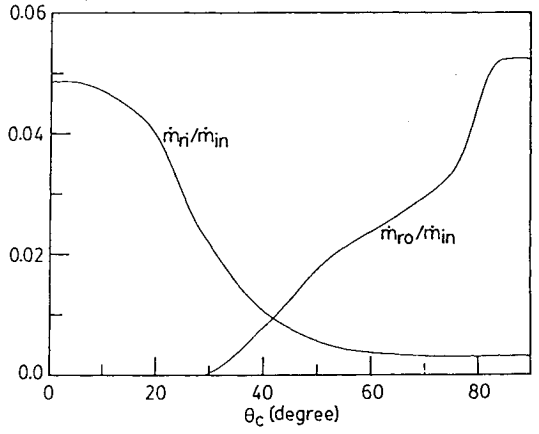

Fig. 8 Aximuthal distribution of various mass flow rates.

pendency studies could not be undertaken. The $9\times10\times40$ grid density arranged in one-quarter of the combustor studied in Ref. 6 is close to the $12\times11\times25$ grid density adopted in Ref. 14 for the case of modeling solid-propellant duct rocket combustor, and is finer than the grid densities typically used in modeling furnaces and combustors.[15] Typically, convergence required 1000 iterations, and the corresponding CPU time on a CDC-CYBER 180/840 computer system was about 4.5 h.

Results and Discussion

General Flow Pattern

The experimental conditions of Liou and Wu,[6] such as air properties and Reynolds number based on combustor diameter and bulk mean velocity of 2.6×10^4, are used in the present computation. Because the inlet ducts are located symmetrically about two diametrical planes that are perpendicular to each other, only one-quarter of the combustor is solved for.

The calculated flow patterns in planes of constant azimuthal angles $\theta_c = 0$, 45, and 90 deg are presented in Fig. 3. It is obvious that between the dome plate and the inlet jets, i.e., in the dome region, the vortices in planes of $\theta_c = 90$ deg (similarly for 45 deg $\leq \theta_c \leq$ 90 deg) and 0 deg (similarly for 0 deg $\leq \theta_c \leq$ 45 deg), respectively, are rotating in opposite directions. The recirculating flows in the $\theta_c = 90$-deg plane (Fig. 3c) are driven by the upstream bifurcating flow of the jets impinging upon one another and by the shear of the inlet jets. In the $\theta_c = 0$-deg plane, the recirculating flows (Fig. 3a) are formed by the spreadout flow in the radial and upstream directions of jet-jet impingement. Figure 3a further shows that in the $\theta_c = 0$-deg plane, the two opposing flows along the dome plate form a sink at about $X_c^* = 0.7$ and $R_c^* = 0.5$. This observation indicates the three-dimensional nature of the flowfield. The flow pattern in the $\theta_c = 45$-deg plane (Fig. 3b) is a combination of those in the planes of $\theta_c = 90$ deg and $\theta_c = 0$ deg.

A major difference between the axisymmetric and the three-dimensional side-dump combustor flowfield is that, in addition to flow upstream and downstream in the former case, the inlet jets can flow in two opposite azimuthal directions for the latter case. The circumferential motion may have important effects on the combustion characteristics because of the en-

hanced mixing associated with these axial vortices. Figure 4 shows the azimuthal flow structure at various X_c^* planes. The swirling motion is more pronounced in the inlet-jet planes and decays toward the dome plate and further downstream directions. These observations can be quantitatively expressed in terms of swirl intensity distribution (see Appendix), as plotted in Fig. 5. The vortices are generated in the region where the two inlet jets impinge on one another, and the resulting swirling motion is confined within the range of $0 \le X_c^* \le 2$ with a peak swirl intensity of 5.4% at $X_c^* = 0.5$. In addition, from Figs. 3-5, the flow is practically helical and becomes unidirectional for $X_c^* \ge 4.0$. This latter observation is consistent with the reported results.[6]

The total pressure loss (see Appendix) is also an important parameter for combustor design. Figure 6 shows its distribution vs X_c^*. The total pressure loss has been nondimensionalized by the mean kinetic energy of the inlet flow. As one can see, the total pressure loss first increases rapidly, from $K_0 = 52\%$, at $X_c^* = 0.5$ to $K_0 = 74\%$ at $X_c^* = 2.0$, and then increases gradually to $K_0 = 75\%$ at $X_c^* = 4.0$. Thereafter, the total pressure loss increases linearly with increasing X_c^*. The major total pressure loss in the region of $X_c^* < 2$ is partly due to the sudden expansion and partly due to high shear stresses and velocity gradients associated with the inlet-jet impingement, which transfers the mean kinetic energy of the flow to the turbulent kinetic energy. Furthermore, the distribution of the total pressure loss shown in Fig. 6 parallels the distribution of the swirl intensity shown in Fig. 5, because the swirling motion generated in the jet impinging region tends to increase the flow path, hence, the friction loss, and tends to increase the turbulent kinetic energy. As the flow proceeds further downstream, the swirling motion degenerates and, therefore, becomes pipe flow with a linear pressure drop.

Since the fraction of the inlet mas flow that is transported into or our of the dome region ($\dot{m}_{ri}/\dot{m}_{in}$ or $\dot{m}_{ro}/\dot{m}_{in}$) may have important effects on the fluid mixing and the flame stability limits[1] inside a ramjet combustor, plots of $\dot{m}_{ri}$ vs X_c^* and $\dot{m}_{ri}/\dot{m}_{in}$, $\dot{m}_{ro}/\dot{m}_{in}$ vs θ_c are shown in Figs. 7 and 8, respectively; $\dot{m}_{ri}/\dot{m}_{in}$ (Fig. 7) decreases almost linearly from inlet ports ($X_c^* = 0$) to the dome plate ($X_c^* = -1.0$). Figure 8 further shows that fluids flowing into the dome region are mainly along the X_c-R_c planes, whose azimuthal angles range from 0 to 45 deg and that a peak value of 4.8% occurs at $\theta_c = 0$ deg, i.e., the jet impinging plane. In contrast, fluids flowing out of the dome region are largely confined to those planes whose θ_c ranges from 45 to 90 deg, and a peak value of 5.2% occurs at $\theta_c = 90$ deg, i.e., inlet-jet plane. These results agree with the velocity vector plots (Figs. 3 and 4), which show that the recirculating vortices in the above two θ_c ranges are rotating in opposite directions.

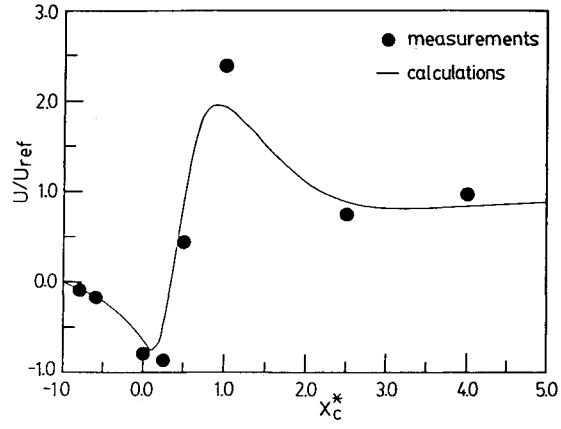

Fig. 9 Calculated and measured distribution of central mean velocities.

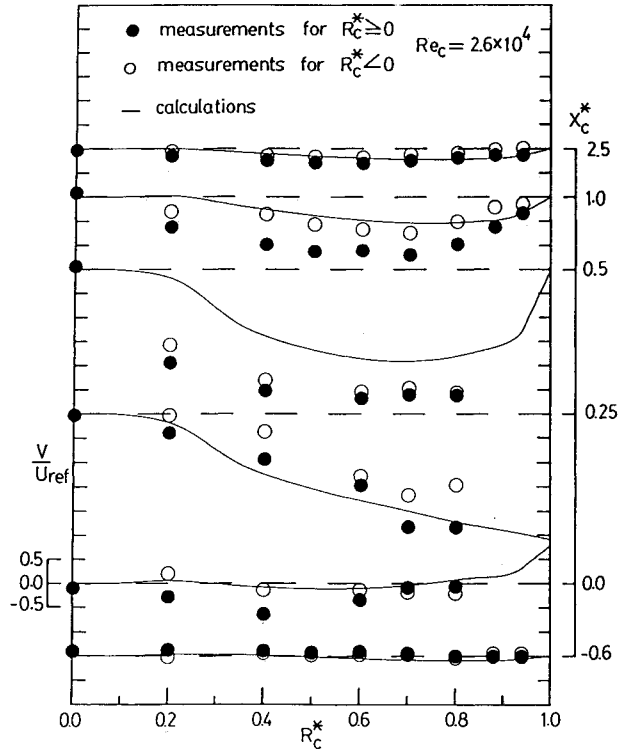

Fig. 10 Calculated and measured mean radial-velocity profiles at various X_c^* for $\theta_c = 90$ deg.

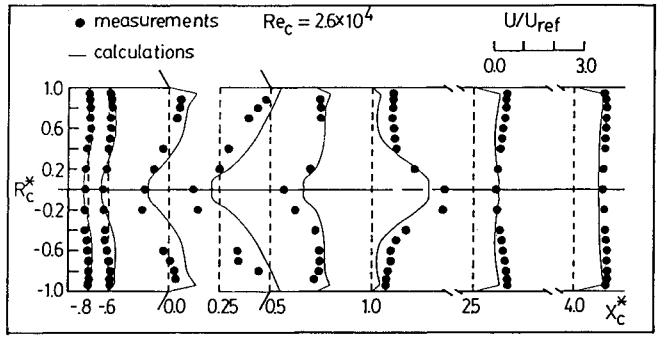

Fig. 11 Calculated and measured mean axial-velocity profiles at various X_c^* for $\theta_c = 90$ deg.

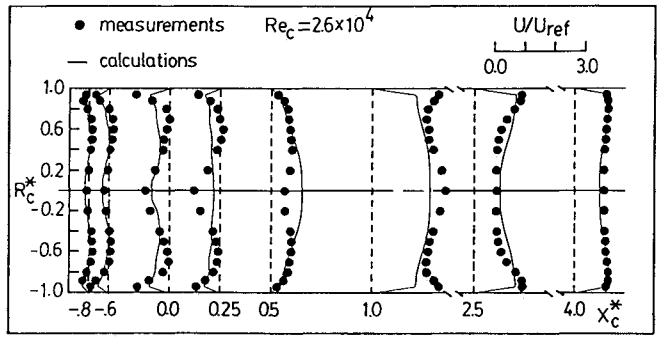

Fig. 12 Calculated and measured mean axial-velocity profiles at various X_c^* for $\theta_c = 90$ deg.

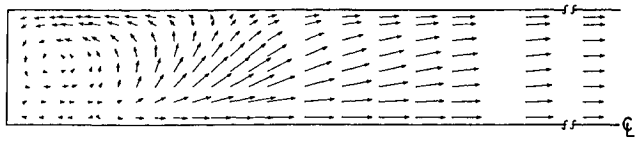

Fig. 13a Vector plot of flow pattern in the $\theta_c = 180$ deg plane.

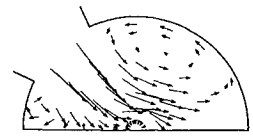

Fig. 14a Vector plot of flow pattern in the inlet cross-sectional plane.

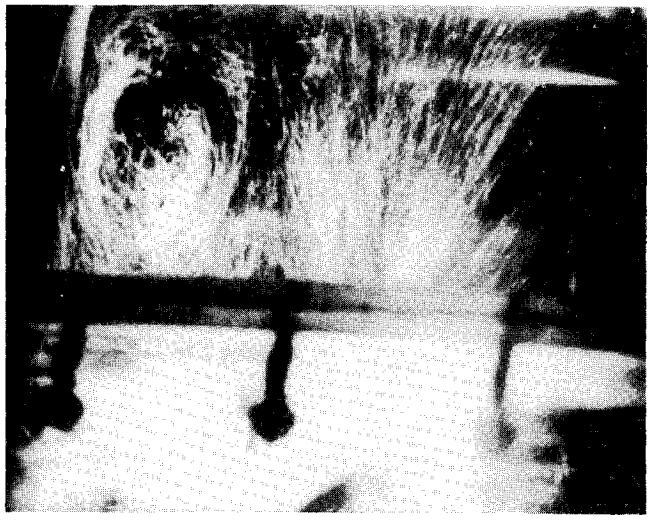

Fig. 13b Corresponding flow visualization photograph.[2]

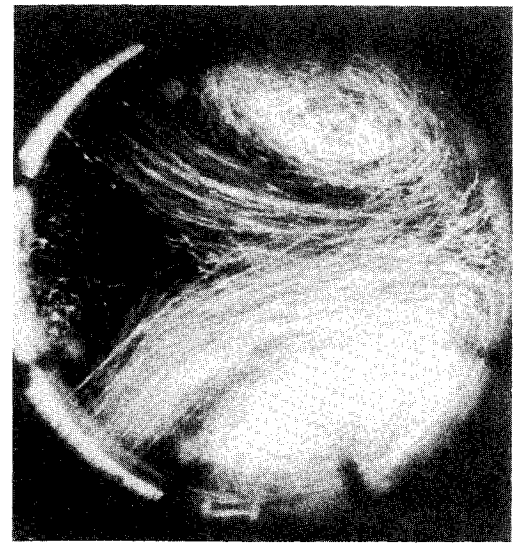

Fig. 14b Corresponding flow visualization photograph.[2]

Comparison with LDV Measurements

Figures 9–12 illustrate the calculated and measured[6] mean velocity profiles throughout the side-dump combustor flowfield. The measured data from $-1 \le R_c^* \le 0$ have been plotted together with those for $0 \le R_c^* \le 1$ in Fig. 10, since the computation is based on the assumption of symmetry about the combustor axis. Also, the comparison is presented for $\theta_c = 0$- and 90-deg planes, since the LDV measurements were made only at these two diametrical planes. The calculated results are in general agreement with LDV data. The centerline mean axial velocity, shown in Fig. 9, is reasonably predicted, and the discrepancies are less than 15% of U_{ref} (= 4.15 m/s) except for $X_c^* = 1.0$ where a discrepancy of 54% U_{ref} is found. The larger discrepancy at $X_c^* = 1.0$ is partly due to the fact that the measured mean velocities reveal highly asymmetric profiles for $0.25 \le X_c^* \le 1.5$, while the calculation assumes a symmetric flow pattern.

Figures 10 and 11 display profiles of the predicted and measured mean radial and axial velocities at various axial stations for $\theta_c = 90$ deg. Discrepancies between predicted and measured profiles decrease toward the dome region and toward the region far downstream ($X_c^* > 1.0$). For $0 \le X_c^* \le 1.0$, the discrepancies are partly due to the symmetry assumption mentioned above and partly due to inaccuracies in the specification of the inlet conditions at the dump plane. In order to mount the rectangular inlet duct on the cylindrical combustion chamber, a 20-mm-thick flange was needed.[5] However, the position of the flange made the LDV measurements at the dump plane impossible. Consequently, the inlet velocity profiles used for calculations were actually measured at a plane of 20 mm above the dump plane. At this measured plane, the flow was characterized by a six-vortex structure in the transverse direction and flow separation in the streamwise direction (near $X_c^* = 0.0$).[5,6] Because of the retardation of the low-speed flow in the dome region, the size of the aforementioned separation zone is increased as the flow arrives at the dump plane. The inlet jet at the dump plane is, therefore, compressed toward the downstream edge ($X_c^* = 0.5$) of the inlet port and has a stronger injection velocity than that used in the calculations. The observation above illustrates why the measured jet velocities for $0 \le X_c^* \le 1$, particularly at $X_c^* = 0.5$ and $X_c^* = 1.0$ of Fig. 10 and at $X_c^* = 1.0$ of Fig. 11, are larger than the corresponding calculated results. The dividing streamline of the jet impingement intersects the combustor axis at $X_c^* = 0.46$, as reported in Ref. 6. The same arguement can also be applied to the comparison between the predicted and measured mean axial velocity profiles at various axial stations for $\theta_c = 0$ deg, as shown in Fig. 12. Generally, the discrepancies are less than 15% of U_{ref}. The underprediction of mean axial velocity near the combustor wall ($0.8 \le R_c^* \le 1$) at $X_c^* = 1.0$, 0.25, and 0.0 is partly due to the stronger axial vorticity generated by the stronger injection jet and partly due to the effect of secondary vortices in the inlet ducts for the experimental case.

Comparison with Previous Calculation and Flow Visualization Results

Vanka et al.[3] performed detailed computations of flowfields in side-inlet dump combustors having an angle of 90 deg between the centerlines of the two inlet ducts. The results of their calculations agree qualitatively with the flow/visualization photographs in a water tunnel,[2] except in the dome region where their calculations do not indicate a vortex pattern in the jet impinging plane ($\theta_c = 180$ deg) shown by the flow visualization. A further calculation of the velocity distribution in their combustor configuration, therefore, was undertaken in the current work to check this disagreement. The angle of the side inlets with respect to the combustor axis is 45 deg for their

configuration. Furthermore, the calculations are performed with their flow conditions, i.e., with water properties at a Reynolds number based on the duct diameter of 2.675×10^5 and with a grid system of $10\times11\times35$ (R_c,θ_c,X_c). Because the inlet ducts are located symmetrically about a diametrical plane, only one-half of the combustor is solved for. Figures 13a and 14a display the calculated mean velocity distribution in terms of vector plots in the $\theta_c = 180$ deg plane and in the cross-sectional plane of inlet jets, respectively. The flow pattern in Fig. 13a obtained from the current calculations clearly reveals the vortex pattern indicated by the flow visualization photograph (Fig. 13b) of Stull et al.[2] Moreover, the calculated cross-sectional vortex shown in Fig. 14a is also in good agreement with their photograph (Fig. 14b). Consequently, an improved prediction of the characteristic vortex patterns mentioned above are obtained in the present calculations.

Summary and Conclusions

1) The computed flow patterns have been compared with both LDV data and flow visualization photographs, and the general trends are in good agreement. In most cases, the quantitative discrepancies are less than 15% of U_{ref}.

2) The current calculations have shown an improvement over the previous work in the prediction of the vortex pattern in the dome region.

3) The flowfield in the dome region is mainly composed of recirculating flows with their vortex axes perpendicular to the X_c^*-R_c^* planes. Moreover, the aforementioned recirculating flows for 0 deg$\le\theta_c\le$45 deg and 45 deg$\le\theta_c\le$90 deg are counter-rotating.

4) In contrast, it is found that the helical flows with their axes parallel to the combustor axis are mainly generated in the impinging region of the two inlet jets and decay rapidly toward both the dome and downstream regions. They further degenerate into unidirectional flow at about four times of combustor diameter downstream.

5) The total pressure loss mainly occurs in the region of $X_c^* \le 2$ and is found to closely correlate with the swirl intensity.

6) The maximum fraction of inlet mass flow transported into and out of the dome region occurs in $\theta_c = 0$ and 90 deg planes, respectively. Moreover, the fraction of the inlet mass flow transported into the dome region decreases approximately linearly toward the dome plate.

Appendix

The swirl intensity (SI) and the total pressure loss (K_0) in this study are defined as below:

$$SI(X_c^*) = \frac{\int_{A(X_c^*)} \frac{1}{2}\rho W^2 \boldsymbol{V}\cdot\boldsymbol{N}\,dA}{-\int_{A_{\text{in}}} \frac{1}{2}\rho(U^2+V^2+W^2)\boldsymbol{V}\cdot\boldsymbol{N}\,dA} \tag{A1}$$

where

$\int_{A(X_c^*)} \frac{1}{2}\rho W^2 \boldsymbol{V}\cdot\boldsymbol{N}\,dA$ = the axial flux of the swirling mean kinetic energy at a given X_c^*

$-\int_{A_{\text{in}}} \frac{1}{2}\rho(U^2+V^2+W^2)\boldsymbol{V}\cdot\boldsymbol{N}\,dA$ = the flux of the total mean kinetic energy at inlet

and

$$K_0(X_c^*) = \frac{E_{\text{in}} - E(X_c^*)}{-\int_{A_{\text{in}}} \frac{1}{2}\rho(U^2+V^2+W^2)\boldsymbol{V}\cdot\boldsymbol{N}\,dA} \tag{A2}$$

where

$$E_{in} = -\int_{A_{\text{in}}} [P + \tfrac{1}{2}\rho(U^2+V^2+W^2)]\boldsymbol{V}\cdot\boldsymbol{N}\,dA$$

$$E(X_c^*) = \int_{A(X_c^*)} [P + \tfrac{1}{2}\rho(U^2+V^2+W^2)]\boldsymbol{V}\cdot\boldsymbol{N}\,dA$$

The nonlinear equations of deviated Reynolds stress are given below:

$$\left[\overline{(u_r u_r)}_d - 2\frac{\mu_t}{\rho}\left(\frac{\partial V}{\partial R_c}\right) + \frac{2}{3}k\right]\left[P_k + \bar{P}_k + \epsilon(C_{A1}-1)\right] - \left[P_{rr} + \bar{P}_{rr} - \frac{2}{3}(P_k + \bar{P}_k)\right](1-C_{A2})k = 0 \tag{A3}$$

$$\left[\overline{(u_r u_\theta)}_d - \frac{\mu_t}{\rho}\left(\frac{\partial W}{\partial R_c} + \frac{\partial V}{R_c\partial\theta_c} - \frac{W}{R_c}\right)\right]\left[P_k + \bar{P}_k + \epsilon(C_{A1}-1)\right] - (P_{r\theta} + \bar{P}_{r\theta})(1-C_{A2})k = 0 \tag{A4}$$

$$\left[\overline{(u_r u_x)}_d - \frac{\mu_t}{\rho}\left(\frac{\partial V}{\partial X_c} + \frac{\partial U}{\partial R_c}\right)\right]\left[P_k + \bar{P}_k + \epsilon(C_{A1}-1)\right] - (P_{rx} + \bar{P}_{rx})(1-C_{A2})k = 0 \tag{A5}$$

$$\left[\overline{(u_\theta u_\theta)}_d - 2\frac{\mu_t}{\rho}\left(\frac{\partial W}{R_c\partial\theta_c} + \frac{V}{R_c}\right) + \frac{2}{3}k\right]\left[P_k + \bar{P}_k + \epsilon(C_{A1}-1)\right] - \left[P_{\theta\theta} + \bar{P}_{\theta\theta} - \frac{2}{3}(P_k + \bar{P}_k)\right] \times (1-C_{A2})k = 0 \tag{A6}$$

$$\left[\overline{(u_\theta u_x)}_d - \frac{\mu_t}{\rho}\left(\frac{\partial U}{R_c\partial\theta_c} + \frac{\partial W}{\partial X_c}\right)\right]\left[P_k + \bar{P}_k + \epsilon(C_{A1}-1)\right] - (P_{\theta x} + \bar{P}_{\theta x})(1-C_{A2})k = 0 \tag{A7}$$

$$\left[\overline{(u_x u_x)}_d - 2\frac{\mu_t}{\rho}\left(\frac{\partial U}{\partial X_c}\right) + \frac{2}{3}k\right]\left[P_k + \bar{P}_k + \epsilon(C_{A1}-1)\right] - \left[P_{xx} + \bar{P}_{xx} - \frac{2}{3}(P_k + \bar{P}_k)\right](1-C_{A2})k = 0 \tag{A8}$$

where

$$P_{rr} = -\left[2\overline{(u_r u_r)}_d\left(\frac{\partial V}{\partial R_c}\right) + 2\overline{(u_r u_\theta)}_d\left(\frac{\partial V}{R_c\partial\theta_c} - \frac{W}{R_c}\right) + 2\overline{(u_r u_x)}_d\left(\frac{\partial V}{\partial X_c}\right)\right]$$

$$P_{r\theta} = -\left[\overline{(u_r u_r)}_d\left(\frac{\partial W}{\partial R_c}\right) + \overline{(u_r u_\theta)}_d\left(\frac{\partial W}{R_c\partial\theta_c} + \frac{V}{R_c} + \frac{\partial V}{\partial R_c}\right) + \overline{(u_r u_x)}_d\left(\frac{\partial W}{\partial X_c}\right) + \overline{(u_\theta u_\theta)}_d\left(\frac{\partial V}{R_c\partial\theta_c} - \frac{W}{R_c}\right) + \overline{(u_\theta u_x)}_d\left(\frac{\partial V}{\partial X_c}\right)\right]$$

$$P_{rx} = -\left[\overline{(u_r u_r)}_d\left(\frac{\partial U}{\partial R_c}\right) + \overline{(u_r u_\theta)}_d\left(\frac{\partial U}{R_c\partial\theta_c}\right) + \overline{(u_r u_x)}_d\left(\frac{\partial V}{\partial R_c} + \frac{\partial U}{\partial X_c}\right) + \overline{(u_\theta u_x)}_d\left(\frac{\partial V}{R_c\partial\theta_c} - \frac{W}{R_c}\right) + \overline{(u_x u_x)}_d\left(\frac{\partial V}{\partial X_c}\right)\right]$$

$$P_{\theta\theta} = -\left[2(\overline{u_r u_\theta})_d\left(\frac{\partial W}{\partial R_c}\right) + 2(\overline{u_\theta u_\theta})_d\left(\frac{\partial W}{R_c\partial\theta_c} + \frac{V}{R_c}\right) + 2(\overline{u_\theta u_x})_d\left(\frac{\partial W}{\partial X_c}\right)\right]$$

$$P_{\theta x} = -\left[(\overline{u_r u_\theta})_d\left(\frac{\partial U}{\partial R_c}\right) + 2(\overline{u_r u_x})_d\left(\frac{\partial W}{\partial R_c}\right) + (\overline{u_\theta u_\theta})_d\left(\frac{\partial U}{R_c\partial\theta_c}\right) + (\overline{u_\theta u_x})_d\left(\frac{\partial U}{\partial X_c} + \frac{\partial W}{R_c\partial\theta_c} + \frac{V}{R_c}\right) + (\overline{u_x u_x})_d\left(\frac{\partial W}{\partial X_c}\right)\right]$$

$$P_{xx} = -\left[2(\overline{u_r u_x})_d\left(\frac{\partial U}{\partial R_c}\right) + (\overline{u_\theta u_x})_d\left(\frac{\partial U}{R_c\partial\theta_c}\right) + 2(\overline{u_x u_x})_d\left(\frac{\partial U}{\partial X_c}\right)\right]$$

$$P_k = (P_{rr} + P_{\theta\theta} + P_{xx})/2$$

$$\bar{P}_{rr} = \frac{\mu_t}{\rho}\left[4\left(\frac{\partial V}{\partial R_c}\right)^2 + 2\left(\frac{\partial V}{R_c\partial\theta_c} - \frac{W}{R_c}\right)^2 + 2\left(\frac{\partial V}{\partial X_c}\right)^2 + 2\left(\frac{\partial W}{\partial R_c}\right)\left(\frac{\partial V}{R_c 2\theta_c} - \frac{W}{R_c}\right) + 2\left(\frac{\partial U}{\partial R_c}\right)\left(\frac{\partial V}{\partial X_c}\right)\right]$$

$$\bar{P}_{r\theta} = \frac{\mu_t}{\rho}\left[2\left(\frac{\partial W}{\partial R_c}\right)\left(\frac{\partial V}{\partial R_c}\right) + \left(\frac{\partial W}{R_c\partial\theta_c} + \frac{V}{R_c} + \frac{\partial V}{R_c\partial\theta_c}\right)\times\left(\frac{\partial W}{\partial R_c} + \frac{\partial V}{R_c\partial\theta_c} - \frac{W}{R_c}\right) + \left(\frac{\partial W}{\partial X_c}\right)\left(\frac{\partial U}{\partial R_c} + \frac{\partial V}{\partial X_c}\right) + 2\left(\frac{\partial V}{R_c\partial\theta_c} - \frac{W}{R_c}\right)\left(\frac{\partial W}{R_c\partial\theta_c} + \frac{V}{R_c}\right) + \left(\frac{\partial V}{\partial X_c}\right)\left(\frac{\partial W}{\partial X_c} + \frac{\partial U}{R_c\partial\theta_c}\right)\right]$$

$$\bar{P}_{rx} = \frac{\mu_t}{\rho}\left[2\left(\frac{\partial U}{\partial R_c}\right)\left(\frac{\partial V}{\partial X_c}\right) + \left(\frac{\partial U}{R_c\partial\theta_c}\right)\left(\frac{\partial V}{R_c\partial\theta_c} - \frac{W}{R_c} + \frac{\partial W}{\partial R_c}\right) + \left(\frac{\partial U}{\partial X_c} + \frac{\partial V}{\partial R_c}\right)\left(\frac{\partial U}{\partial R_c} + \frac{\partial V}{\partial X_c}\right) + \left(\frac{\partial V}{R_c\partial\theta_c} - \frac{W}{R_c}\right)\left(\frac{\partial W}{R_c\partial\theta_c} + \frac{V}{R_c}\right) + 2\left(\frac{\partial V}{\partial X_c}\right)\left(\frac{\partial U}{\partial X_c}\right)\right]$$

$$\bar{P}_{\theta\theta} = \frac{\mu_t}{\rho}\left[2\left(\frac{\partial W}{\partial R_c}\right)^2 + 4\left(\frac{\partial W}{R_c\partial\theta_c} + \frac{V}{R_c}\right)^2 + 2\left(\frac{\partial W}{\partial X_c}\right)^2 + 2\left(\frac{\partial W}{\partial R_c}\right)\left(\frac{\partial V}{R_c\partial\theta_c} - \frac{W}{R_c}\right) + 2\left(\frac{\partial V}{\partial X_c}\right)\left(\frac{\partial U}{R_c\partial\theta_c}\right)\right]$$

$$\bar{P}_{\theta x} = \frac{\mu_t}{\rho}\left[\left(\frac{\partial U}{\partial R_c}\right)\left(\frac{\partial V}{R_c\partial\theta_c} + \frac{W}{R_c} + \frac{\partial W}{\partial R_c}\right) + \left(\frac{\partial W}{\partial R_c}\right)\left(\frac{\partial U}{\partial R_c} + \frac{\partial V}{\partial X_c}\right) + 2\left(\frac{\partial U}{R_c\partial\theta_c}\right)\left(\frac{\partial W}{R_c\partial\theta_c} + \frac{V}{R_c}\right) + \left(\frac{\partial U}{\partial X_c} + \frac{\partial W}{R_c\partial\theta_c} + \frac{V}{R_c}\right)\left(\frac{\partial U}{R_c\partial\theta_c} + \frac{\partial W}{\partial X_c}\right) + 2\left(\frac{\partial W}{\partial X_c}\right)\left(\frac{\partial U}{\partial X_c}\right)\right]$$

$$\bar{P}_{xx} = \frac{\mu_t}{\rho}\left[2\left(\frac{\partial U}{\partial R_c}\right)^2 + 2\left(\frac{\partial U}{R_c\partial\theta_c}\right)^2 + 4\left(\frac{\partial U}{\partial X_c}\right)^2 + 2\left(\frac{\partial U}{\partial R_c}\right)\times\left(\frac{\partial V}{\partial X_c}\right) + 2\left(\frac{\partial W}{\partial X_c}\right)\left(\frac{\partial U}{R_c\partial\theta_c}\right)\right]$$

$$\bar{P}_k = (\bar{P}_{rr} + \bar{P}_{\theta\theta} + \bar{P}_{xx})/2$$

That is,

$$\bar{P}_{ij} = -\left[(\overline{u_i u_m})_B\frac{\partial U_j}{\partial X_m} + (\overline{u_j u_m})_B\frac{\partial U_i}{\partial X_m}\right]$$

$$P_{ij} = -\left[(\overline{u_i u_m})_d\frac{\partial U_j}{\partial X_m} + (\overline{u_j u_m})_d\frac{\partial U_i}{\partial X_m}\right]$$

$$\bar{P}_k = \tfrac{1}{2}\bar{P}_{ii}$$

$$P_k = \tfrac{1}{2}P_{ii}$$

References

[1]Shahaf, M., Goldman, Y., and Greenberg, J. B., "An Investigation of Impinging Jets in Flow with Sudden Expansion," *Proceedings of the 22nd Israel Annual Conference on Aviation and Astronautics*, Israel Ministry of Transport, Haifa, Israel, March 1980, pp. 100-106.

[2]Stull, F. D., Craig, R. R., Wtreby, G. D., Vanka, S. P., "Investigations of a Dual Inlet Side Dump Combustor Using Liquid Injection," *Journal of Propulsion and Power*, Vol. 1, Jan.-Feb. 1985, pp. 83-86.

[3]Vanka, S. P., Stull, F. D., and Craig, R. R., "Analytical Characterization of Flow Fields in Side Inlet Dump Combustors," AIAA Paper 83-1399, June 1983.

[4]Vanka, S. P., Craig, R. R., and Stull, F. D., "Mixing, Chemical Reaction and Flow Field Development in Ducted Rockets," AIAA Paper 85-1271, July 1985.

[5]Liou, T.-M. and Wu, S.-M., "Application of Laser Velocimetry to the Curved Inlet Duct," *Third International Symposium on Application of Laser-Doppler Anemometry to Fluid Mechanics*, Ladon-Instituto Superior Technico, Lisbon, Portugal, July 1986, pp. 9.3.1-9.3.6.

[6]Liou, T.-M. and Wu, S.-M., "Flow Field in a Dual-Inlet Side-Dump Combustor," *Journal of Propulsion and Power*, Vol. 4, Jan.-Feb. 1988, pp. 53-60.

[7]Ljuboja, M. and Rodi, W., "Calculation of Turbulent Wall Jets with an Algebraic Reynolds Stress Model," *Journal of Fluids Engineering*, Vol. 102, Sept. 1980, pp. 350-356.

[8]Hinze, J. O., *Turbulence*, McGraw-Hill, New York, 1959, pp. 22-24.

[9]Launder, B. E. and Spalding, D. B., "The Numerical Computation of Turbulence Flows," *Computer Methods in Applied Mechanics and Engineering*, Vol. 3, 1974, pp. 269-289.

[10]Launder, B. E., Reece, G. J., and Rodi, W., "Progress in the Development of a Reynolds Stress Turbulence Closure," *Journal of Fluid Mechanics*, Vol. 68, Pt. 3, 1975, pp. 537-566.

[11]Patankar, S. V. and Spalding, D. B., "Calculation Procedure for Heat, Mass, and Momentum Transfer in Three-Dimensional Parabolic Flows," *International Journal of Heat and Mass Transfer*, Vol. 15, Sept. 1972, pp. 1787-1806.

[12]Patankar, S. V., *Numerical Heat Transfer and Fluid Flow*, Hemisphere, New York, 1980.

[13]Dennis, J. E., Jr., and Schnahel, R. B., *Numerical Methods for Unconstrained Optimization and Nonlinear Equations*, Prentice-Hall, Englewood Cliffs, New Jersey, 1983.

[14]Cherng, D. L., Yang, V., and Kuo, K. K., "Simulations of Three-Dimensional Turbulent Reacting Flows in Solid-Propellant Ducted Rocket Combustors," AIAA Paper 88-3042, July 1988.

[15]Khalil, E. E., *Modeling of Furnaces and Combustors*, Abacus Press, Kent, OH, 1982.